Competing Symmetries and Broken Bonds in Superconducting Vortex-Antivortex Molecular Crystals

J. S. Neal, M. V. Milošević,* and S. J. Bending†
Department of Physics, University of Bath, Claverton Down, Bath BA2 7AY, United Kingdom

A. Potenza,‡ L. San Emeterio, and C. H. Marrows
School of Physics and Astronomy, University of Leeds, Leeds LS2 9JT, United Kingdom
(Received 20 March 2007; published 17 September 2007)

Hall probe microscopy has been used to image vortex-antivortex molecules induced in superconducting Pb films by the stray fields from square arrays of magnetic dots. We have directly observed spontaneous vortex-antivortex pairs and studied how they interact with added free (anti)fluxons in an applied magnetic field. We observe a variety of phenomena arising from competing symmetries which either drive added antivortices to join antivortex shells around dots or stabilize the translationally symmetric antivortex lattice between the dots. Added vortices annihilate antivortex shells, leading first to a stable ''nulling state'' with no free fluxons and then, at high densities, to vortex shells around the dots stabilized by the asymmetric antipinning potential. Our experimental findings are in good agreement with Ginzburg-Landau calculations.

DOI: 10.1103/PhysRevLett.99.127001 PACS numbers: 74.78.Na, 74.20.De, 74.25.Ha

Two-dimensional ordering and crystallization of particles on structured substrates has attracted considerable attention in the past decade. For example, the rich crystalline states of colloidal particles have been examined both theoretically and experimentally [1], as well as the ordering of atoms on corrugated surfaces [2] and vortices in superconductors with periodic pinning arrays [3]. In such cases particles are grouped at substrate potential minima, and each of these groups can act as a single particle with internal degrees of rotational freedom, forming states that have additional long-range translational order. The existence of these competing symmetries gives rise to particularly subtle phenomena and leads to ordered states which are analogous to ''molecular crystals.''

The question of crystallization becomes particularly interesting when single species molecules are replaced by ionic ones containing positive and negative counterparts. Recently, colloidal crystals of oppositely charged particles have been experimentally realized [4]. Surprisingly, it was found that the stoichiometry of such crystals is not dictated by charge neutrality, allowing the formation of a diverse range of binary structures, which gradually melted upon application of an electric field. Analogous ''ionic'' structures can be found in superconductors, specifically in superconducting films deposited on spatial arrays of magnets. Each magnet may generate one or more spontaneous vortex-antivortex (VAV) pairs in the superconducting film. These either remain associated with individual magnets as VAV ''molecules'' [5] in dilute arrays, or organize themselves into an ionic crystal in dense arrays [6]. To date there has been no experimental verification of such spontaneous VAV structures, which is the first objective of this Letter. Exactly how VAV molecules transform into lattices (analogous to ionic colloidal crystals) and how they interact with (anti)fluxons introduced by external magnetic fields remain challenging questions for both theory and experiment, and this work yields critical insights in these areas.

In this Letter, we directly study VAV structures in a Pb superconducting film deposited on a square array of magnetic dots with perpendicular magnetization (see Fig. 1), in an applied homogeneous magnetic field. Superconductor-ferromagnet hybrid systems can be broadly divided into two classes—those where magnetic nanostructures with weak moments are used as pinning sites to enhance the superconducting critical current by suppressing flux line motion [7], and those with strong moments which lead to the spontaneous formation of VAV pairs. The latter have been found to enhance the critical temperature of the film at finite magnetic field through field compensation effects [8]. While such considerations are valid near the superconductor-normal phase boundary, where screening can be neglected ($j_c \approx 0$), the situation deep within the superconducting state is qualitatively different owing to the requirement for magnetic flux to be quantized. Here a

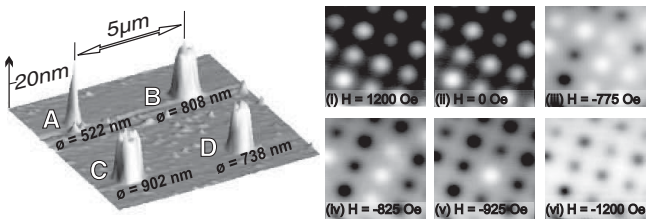

FIG. 1. Atomic force microscope image of the magnetic disk array (left) and (i)–(vi) SHPM images of magnetization reversal (scan range is $\sim 17\ \mu\text{m} \times 17\ \mu\text{m}$ at 20 K). The gray scale of images (i) and (ii) spans 2.66 G and 2.63 G, respectively (see text).

simple picture of field cancellation is no longer applicable and a microscopic picture of the formation of spontaneous VAV pairs is essential along with an understanding of annihilation and trapping processes. This is a regime where, to date, very few experimental studies have been made (cf. [9]).

To address the important outstanding issues in the low-temperature regime, we have performed high spatial resolution scanning Hall probe microscopy (SHPM) [10] on hybrid samples deep inside the superconducting state ($0.67 < T/T_c < 1$). The samples investigated consisted of a 1.5 mm $\times$ 1.5 mm array of ferromagnetic disks covered with a type II superconducting Pb film. The disks were formed in a $[\mathrm{Co}(0.5\ \mathrm{nm})/\mathrm{Pt}(1\ \mathrm{nm})]_{12}$ multilayer film sputtered on a $\mathrm{Si}/\mathrm{SO}_2$ substrate with uniaxial perpendicular magnetic anisotropy. They were patterned by electron beam lithography and reactive ion etching through an evaporated Al etch mask. Four different diameter circular disks with different magnetic moments were patterned on the corners of a 5 μm $\times$ 5 μm square cell which was repeated periodically in a square lattice, allowing the behavior of dots with different spontaneous VAV numbers to be compared in the same sample. Design diameters of 522 nm (dot A), 738 nm (D), 808 nm (B), and 902 nm (C) were chosen, corresponding theoretically to 1, 3, 3, and 5 spontaneous VAVs, respectively [5]. Figure 1 shows an atomic force micrograph of the unit cell of the disk array. The magnetization of the unpatterned Co/Pt film was measured by the Magneto-Optical Kerr Effect at 300 K and shown to have high remanence and a coercive field of $\sim$1000 Oe. Figure 1 shows SHPM images of magnetization reversal in the disks at $T = 20$ K, indicating a range of coercive fields spanning 700–1000 Oe and magnetic saturation above $\sim \pm 1000$ Oe. Switching of the weakly coupled disks is largely uncorrelated, but once magnetized, disks of a given size exhibit very strong remanence at $H = 0$ and remain in a single domain state with highly uniform out-of-plane moments. The disks were coated with a 20 nm Ge layer to suppress proximity effects and an 80 nm Pb film deposited using dc magnetron sputtering followed by a 10 nm Mo capping layer to prevent oxidation. Magnetization measurements on a single Pb film of the same thickness indicate that it is a type II superconductor with $T_c = 6.68$ K, $\lambda_{\mathrm{eff}}(5\ \mathrm{K}) \approx 120$ nm, and $\xi(5\ \mathrm{K}) \approx 50$ nm. Finally the sample was also coated with 20 nm Ge and 50 nm Au to enhance the stability of the SHPM when in tunneling contact. Microscopy was performed in a 7 T superconducting magnet at $T = 5$ K with a $\sim$0.5 μm spatial resolution GaAs/AlGaAs Hall sensor. Prior to imaging the Co/Pt dots were magnetized to saturation in an applied magnetic field of 3000 Oe. An unwanted consequence of this was a small amount of trapped magnetic flux in our superconducting solenoid, with a remanent field ≈ -3.5 Oe acting in the opposite direction to the (positive) dot magnetization. This "background field" is estimated from a comparison between images and simulations (cf. spontaneous VAVs in Fig. 2 and also the "nulling"

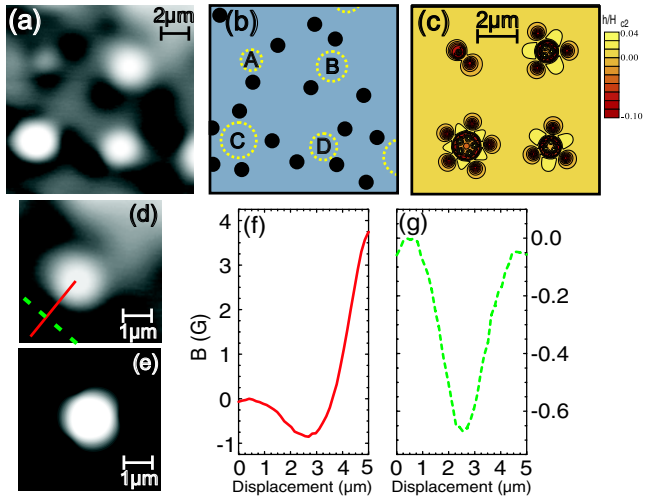

FIG. 2 (color online). SHPM image of spontaneous VAV configurations at $H_a = 3.5$ Oe ($H_{\mathrm{eff}} \approx 0$) and $T = 5$ K (a) and a schematic depiction of the AV locations (b) (dashed circles indicate the locations of magnetic disks). (c) Map of magnetic induction across theoretically predicted VAV configurations. (d), (e) Magnetic induction map across dot B, experiment (d) vs theory (e). (f), (g) Induction profiles across one AV along the lines indicated in (d).

state) and creates a constant offset to our applied field (H_a) axis in all cases. Defining the actual applied field as H_{eff} ($\cong H_a - 3.5$ Oe) there are two noteworthy field conditions—the spontaneous VAV state when $H_{\mathrm{eff}} = 0$, and a nulling state (H_{null}) when all the spontaneous AVs have been exactly annihilated by externally added flux quanta. For $H_{\mathrm{eff}} < 0$ we have excess "free" AVs, for $0 < H_{\mathrm{eff}} < H_{\mathrm{null}}$ we have a gradual annihilation of spontaneous AVs, and for $H_{\mathrm{eff}} > H_{\mathrm{null}}$ we have free vortices.

Zero effective applied field.—We focus first on spontaneous VAV configurations at $H_{\mathrm{eff}} \approx 0$. Figure 2(a) shows the first direct observation of spontaneous VAV shell structures. A strongly nonlinear gray scale has been used to enhance identification of AVs. This can lead to apparent variations in AV intensity due to small variations in, e.g., scan height, but does not influence our analysis which is based on identification of discrete fluxons. This SHPM image maps the full scan range of our microscope (12 μm $\times$ 12 μm) and, in common with all other images presented here, was obtained after field-cooling. As expected, the (black) AVs clearly order in shell-like structures around the magnetic dots, while (white) vortices remain confined above the dots. Careful line-scan analysis allows one to determine the exact locations of AVs and these are sketched for clarity in Fig. 2(b). Figure 2(c) illustrates the results of Ginzburg-Landau (GL) simulations for our exact sample geometry, obtained with coherence length $\xi(0) = 50$ nm and uniform magnetization of the dots of $M = 750$ G. Three-dimensional calculations have also been performed to investigate the role of the topography introduced by the underlying disk array (for details of the approach we refer to Ref. [6]). The experi-

mentally observed vorticity is in good agreement with simulations and, broadly speaking, increases with the magnetic moment of the disks (subject to flux quantization). Moreover, the agreement between experiment and theory is further apparent in Figs. 2(d) and 2(e), which compare magnetic induction maps across magnet B. To highlight the structure of one of the bound AVs, Figs. 2(f) and 2(g) show line scans of the induction profile in the two indicated orthogonal directions.

Negative effective applied fields.—Figure 3 illustrates the effect of introducing additional "free" AVs into the system by applying negative effective applied fields, $H_{\text{eff}} < 0$. Panel (a) shows the "difference" image obtained after subtracting image 2 at $H_{\text{eff}} \approx -1$ Oe from image 1 at $H_{\text{eff}} \approx 0$ Oe. White spots in the difference image represent either unmatched AVs or "annihilated" Vs in image 2. We see that two new AVs occupy interstitial sites between magnets while a third one joins the AV shell around dot D. The fourth remaining white spot cannot be associated with an AV, since it is located under the magnet itself. We conclude that together with the adjacent black spot it represents a VAV pair which has collapsed. In other words, the 738 nm magnetic dot (D), which induced 3 VAV pairs at $H_{\text{eff}} \approx 0$ Oe, now generates only two in the sample at $H_{\text{eff}} \approx -1$ Oe. In Figs. 3(b)–3(e) we present a series of GL simulations to clarify this point. These illustrate Cooper-pair density plots obtained at $H_{\text{eff}} = 0$, -0.6, -1, and -1.8 Oe, respectively.

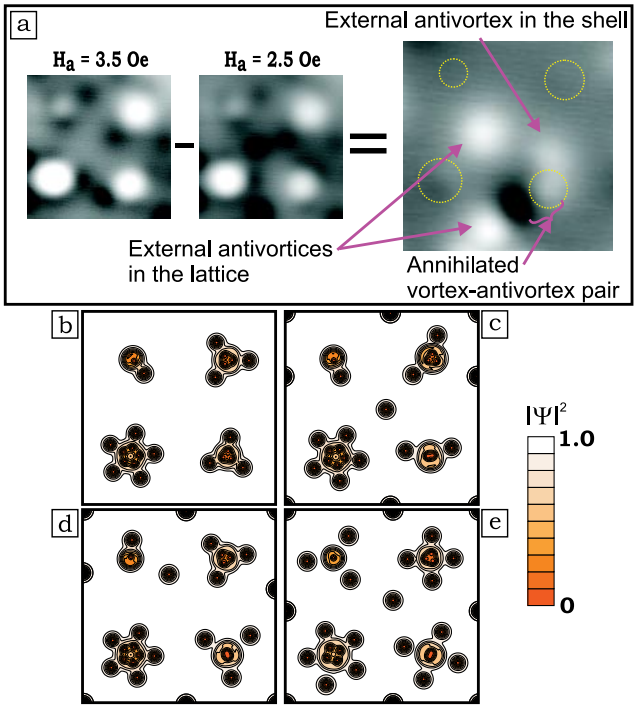

FIG. 3 (color online). (a) SHPM images obtained at two different effective applied fields imaged at $T = 5$ K and their difference image (see text). (b)-(e) Cooper-pair density plots obtained theoretically for applied fields $H_{\text{eff}} = 0$, -0.6, -1, and -1.8 Oe, respectively.

These figures clearly illustrate how the square symmetry of the underlying magnetic lattice imposes itself on the natural shell structure of the individual VAV molecules. For example, in Fig. 3(c), with 3 added external AVs, one of the spontaneous AVs detaches from magnet B and joins the interstitial AV lattice. Effectively, a spontaneous VAV bond is broken, as the AV opts for the mutual interaction with other AVs rather than with its positive counterpart. In a reversal of this scenario for a larger number of external AVs [e.g., 5 in Fig. 3(d)], the excess AV, not needed in the interstitial lattice, approaches dot D, attracted by the positive core, and joins the AV shell. This does not, however, mean that the shell AV structure prevails over the square lattice. Quite the contrary, the new negatively charged VAV molecule now acts as a single component of the lattice. This is best illustrated in Fig. 3(e) (with nine external AVs), where all molecules have negative net charge ($A : -2$, $B : -1$, $C : -1$, $D : -2$).

Positive effective applied fields.—The general behavior of the VAV molecular crystal in a positive applied field is more intuitive, as it is mainly governed by the annihilation between AV shells and externally added vortices. With increasing applied field, each of the molecules progressively loses its negative "ions" and becomes positively charged. However, even after all AVs are annihilated, the vortex "charge" of individual magnetic dots keeps increasing due to the attraction between a magnet and a vortex when their moments are parallel [11]. This is emphasized in Fig. 4, where we show the number of experimentally measured off-site fluxons as a function of applied field, as well as the results of GL calculations. Both plots clearly show a nulling field ($H_a \approx 6$ Oe), where we have no free fluxons. Importantly we find that this condition is met for a

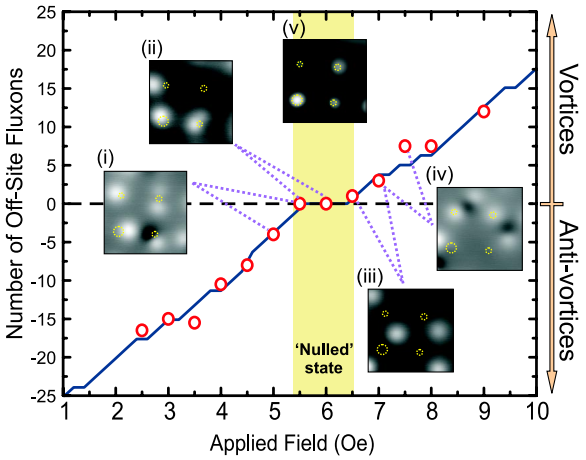

FIG. 4 (color online). Number of experimentally observed free (anti)vortices vs applied magnetic field (open dots) at $T = 5$ K. Solid line shows the predictions of GL theory (shifted by $+4$ Oe on the field axis to simulate flux trapping in solenoid). (i)-(iv) Experimental SHPM difference images constructed between the indicated fields (see text). $\Delta H = 0.5$ Oe corresponds to $\sim 3\phi_0$ per field-of-view on average. (v) Experimental SHPM image of the "nulling" state ($H_a = 5.5$ Oe).

range of applied fields, i.e., $\Delta H_a \geq 1$ Oe. This "locking" behavior, which arises due to the change in vortex occupation number of the magnetic disks, ensures the absence of any off-site fluxons, and consequently enhances the critical current of the sample. The asymmetry of our magnetic array cell is actually very beneficial here, as it ensures pinning of all individual vortices added to the system and prevents their off-site ordering for noncommensurate numbers (so-called fractional matching).

Upon further increase of applied field, the nonuniform changes in on-site vortex occupation across the sample impact on off-site vortices. The potential landscape for the pinning of "free" interstitial vortices becomes "dynamic" since interactions with pinned vortex molecules relocate the energy minima as their charge changes. All the above effects are illustrated in the series of difference images, Figs. 4(i), 4(ii), 4(iii), and 4(iv), between the two indicated successive field-cooled states. Figure 4(i) shows the annihilation of AVs (white spots) together with a decrease in the vortex occupation number of dot D (black spot). Figure 4(ii) shows the change in occupation of the two lower disks near H_{null} (white spots), Fig. 4(iii) shows the crystallization of interstitial vortices (white spots), and Fig. 4(iv) shows the interaction-driven movement of vortices (adjacent pairs of black and white spots). Note that the off-center incorporation of new on-site vortices in Fig. 4(ii) is strongly indicative of a multivortex state above magnetic disks, in agreement with GL calculations.

Further proof that these phenomena arise due to competing interactions and not disorder is given in Fig. 5, which illustrates interstitial vortex structures at larger positive magnetic fields. At sufficiently large magnetic fields a square interstitial vortex lattice is recovered [Fig. 5(a)], mirroring conventional matching phenomena. However, the occupation number of the vortex molecules at each of the dots is different ($A:2$, $B:5$, $C:6$, $D:4$), which slightly distorts the lattice. The influence of multiquanta vortices at the magnet sites becomes more evident at still higher vortex densities. The presence of four different repulsive potentials propagating radially from the corners of the square cell and strong interactions between interstitial vortices result in their arrangement in shells [cf. Fig. 5(b)]. Such an unusual ordering of vortices was never observed in the presence of uniform pinning. While AVs form shells around confined vortices due to their mutual attraction, uniquely and counterintuitively, vortex shells are formed by repulsion. The same scenario applies generally to any system of interacting particles in a similar environment. Moreover, the complex VAV interactions demonstrated in this Letter should also be reflected in two-component colloidal suspensions with oppositely charged particles, e.g., coated by charged polymers [12].

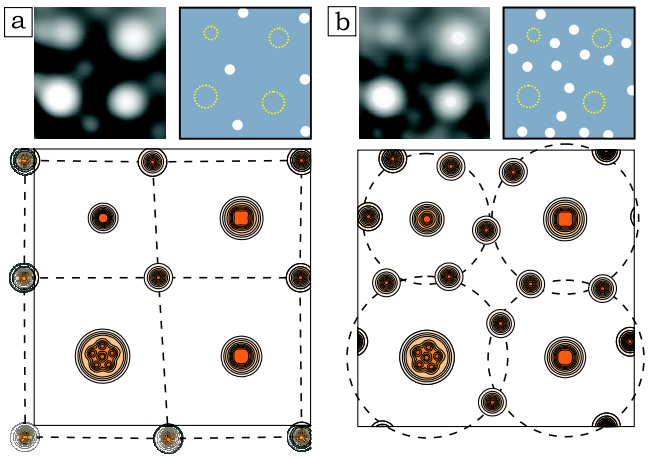

FIG. 5 (color online). SHPM images at $T = 5$ K and corresponding Cooper-pair density plots illustrating formation of (a) an interstitial vortex lattice ($H_{\text{eff}} \approx 4.5$ Oe) and (b) interstitial vortex shells for high vortex densities ($H_{\text{eff}} \approx 7.5$ Oe).

In conclusion, we have directly imaged spontaneous VAV shell structures induced in superconducting films by the stray fields of magnetic arrays for the first time. We observe a variety of subtle phenomena which arise from competition between the n-fold rotational symmetry of the VAV molecules and the translationally symmetric lattice of magnets. Our measurements agree with GL calculations and give unique insights into the properties of ionic crystals based on the ordering of binary systems of particles, e.g., oppositely charged colloidal particles.

This work was supported by UK-EPSRC grants No. GR/D034264/1 and No. Gr/P02707/1. M. V. M. acknowledges support from the EU Marie-Curie Intra-European program.

*Also at: Departement Fysica, Universiteit Antwerpen, Groenenborgerlaan 171, B-2020 Antwerpen, Belgium.
†s.bending@bath.ac.uk
‡Current address: Diamond Light Source Ltd, Diamond House, Chilton, Didcot, Oxfordshire, OX11 0DE, UK.

[1] C. Reichhardt and C. J. Olson, Phys. Rev. Lett. **88**, 248301 (2002); M. Brunner and C. Bechinger, Phys. Rev. Lett. **88**, 248302 (2002).
[2] P. Zeppenfeld *et al.*, Phys. Rev. Lett. **78**, 1504 (1997).
[3] K. Harada *et al.*, Science **274**, 1167 (1996).
[4] M. E. Leunissen *et al.*, Nature (London) **437**, 235 (2005).
[5] M. V. Milošević and F. M. Peeters, Phys. Rev. B **68**, 024509 (2003).
[6] M. V. Milošević and F. M. Peeters, Phys. Rev. Lett. **93**, 267006 (2004); D. J. Priour, Jr. and H. A. Fertig, Phys. Rev. Lett. **93**, 057003 (2004).
[7] J. I. Martin *et al.*, Phys. Rev. Lett. **79**, 1929 (1997); D. J. Morgan *et al.*, Phys. Rev. Lett. **80**, 3614 (1998).
[8] S. A. Wolf *et al.*, Phys. Rev. B **25**, 1990 (1982); H. W. Meul *et al.*, Phys. Rev. Lett. **53**, 497 (1984); M. Lange *et al.*, Phys. Rev. Lett. **90**, 197006 (2003).
[9] M. Lange *et al.*, Phys. Rev. B **72**, 052507 (2005).
[10] A. Oral *et al.*, Appl. Phys. Lett. **69**, 1324 (1996).
[11] S. Erdin *et al.*, Phys. Rev. B **66**, 014414 (2002); M. V. Milošević and F. M. Peeters, Phys. Rev. B **68**, 094510 (2003); for review, see I. F. Lyuksyutov and V. L. Pokrovsky, Adv. Phys. **54**, 67 (2005).
[12] F. Caruso *et al.*, Macromolecules **32**, 2317 (1999).